Optical properties of Mn-Co-Ni-O thin films prepared by radio frequency sputtering deposition

Wei Zhou,[1,2] Jing Wu,[1,2] Cheng Ouyang,[1,2] Yanqing Gao,[1,2] Xiaofeng Xu,[3] and Zhiming Huang[1,2,a)]

[1]*National Laboratory for Infrared Physics, Shanghai Institute of Technical Physics, CAS, 500 Yutian Road, Shanghai 200083, People's Republic of China*

[2]*Key Laboratory of Space Active Opto-Electronics Technology, Shanghai Institute of Technical Physics, CAS, 500 Yutian Road, Shanghai 200083, People's Republic of China*

[3]*College of Science, Donghua University, 2999 Renmin Bei Road, Shanghai 201620, People's Republic of China*

(Received 23 December 2013; accepted 20 February 2014; published online 7 March 2014)

$Mn_{1.4}Co_{1.0}Ni_{0.6}O_4$ (MCN) thin films are prepared by RF sputtering deposition method on amorphous Al_2O_3 substrate. Microstructure and X-ray photoelectron spectroscopy analyses suggest improvements in crystallinity and stoichiometry for MCN films with post-annealed process. Infrared (IR) optical constants of the MCN films are obtained by IR spectroscopic ellipsometer (SE) in the range of 1500 cm^{-1} to 3200 cm^{-1} (2.8–6.7 μm). The derived effective charge supports the increase of the oxidation after annealing. The dielectric function of the films is also extracted by SE in the range of 300–1000 nm adopting a double Lorentz model together with a Tauc–Lorentz model. The mechanism in electronic transition process is discussed based on the variation observed in the optical absorption spectra of the as-grown and post-annealed samples. The optical absorption peaks located at 1.7 eV, 2.4–2.6 eV, and 3.5–4 eV are attributed to the charge-transfer transitions of 2p electrons of oxygen ions and 3d electrons of Mn and Co ions. Our results are very important to understand the optoelectronic mechanism and exploit applications of metal oxides. © *2014 AIP Publishing LLC*. [http://dx.doi.org/10.1063/1.4867439]

I. INTRODUCTION

Transition metal oxides (TMO) have arisen intensive interests in recent years, due to the rich physical phenomena such as metal-insulator transition,[1] superconductivity,[2,3] and ferromagnetism.[4] Spinel compound oxide Mn-Co-Ni-O, as an important TMO semiconductor, has exhibited varied electrical, magnetic, and optical properties, which attracts many research attentions.[5–8] Due to strong electron-phonon coupling, Mn-Co-Ni-O has been widely utilized for its excellent negative temperature coefficient (NTC) features, including infrared detection, surge protection, thermal sensing, and so on.[9,10]

With the development of membrane technology, Mn-Co-Ni-O films have been grown by various kinds of techniques, such as chemical solution deposition (CSD),[11,12] RF sputtering deposition method,[13] screen printing,[14] and laser molecular beam epitaxy method.[15] Among those techniques, RF sputtering method acquires advantages including highly efficiency, low cost, and precise controlling in growth parameters. Therefore, RF sputtering method has high significance in industrial applications. However, only few works devoted to the optical properties of Mn-Co-Ni-O films. Dannenberg *et al.* studied the infrared optical properties of $Mn_{1.56}Co_{0.96}Ni_{0.48}O_4$ thin films on silicon substrate deposited by RF sputtering method under 300–400 °C.[16] They found that optical properties were dependent on the oxygen partial pressure. Until now, there is no study on the affecting of annealing process to the optical constants of Mn-Co-Ni-O thin films. In this paper, we investigate for the first time the ultraviolet-visible-near infrared (UV-VIS-NIR) and infrared optical constants by spectroscopic ellipsometry for the as-grown and post-annealed $Mn_{1.4}Co_{1.0}Ni_{0.6}O_4$ (MCN) films.

II. EXPERIMENTAL DETAILS

$Mn_{1.4}Co_{1.0}Ni_{0.6}O_4$ powders were synthesized by reacting a stoichiometric mixture of $Mn(CH_3COO)_2{\cdot}4H_2O$, $Co(CH_3COO)_2{\cdot}4H_2O$, $Ni(CH_3COO)_2{\cdot}4H_2O$, with an atomic ratio of 7:5:3 and then calcining it at 1100 K for 4 h. A wafer sized Φ 60 mm × 4 mm was prepared via traditional sintering method. MCN films were prepared on amorphous Al_2O_3 substrate by RF (13.56 MHz) sputtering method with a conventional off-axis setup, using commercial RF sputtering system JPGF-400-G. Prior to film deposition, the base pressure was evacuated to be approximately 5×10^{-3} Pa, and the working pressure was 0.4 Pa. High purity (>99.99%) argon was applied to provide the plasma. The temperature during growth was set to be 200 °C. MCN films were deposited under 100 W with deposition time of about 1.5 h and then annealed at 750 °C for 90 min.

The phase identification was studied by x-ray diffraction (XRD) in the (θ, 2θ) configuration using a RigaKu D/MAX-2550 x-ray diffractometer with Cu K_α radiation ($\lambda = 1.5418$ Å). The microstructure of the as-grown films was investigated by a Nanoscope IIIa multimode Atomic Force Microscope (AFM) (Bruker, Santa Barbara, CA) in tapping mode. The morphological character of the post-annealed films was studied by HITACHI S-4800 field-emission scanning electron microscope (FESEM). X-ray photoelectron spectroscopy (XPS) spectra were acquired with a Kratos Axis Ultra[DLD]

a)Author to whom correspondence should be addressed. Electronic mail: zmhuang@mail.sitp.ac.cn. Tel.: (+86) 021 25051862.

spectrometer (Shimadzu group company) using a monochromatic Al K_α source (1486.6 eV). The C 1s XPS at 284.6 eV was used for calibration. Infrared ellipsometric measurement was carried out using an infrared SE (SC503, Shanghai Sanco, Inc.) in 2.8–6.7 μm wavelength range with a wavelength interval of 100 nm. The incident angle was set to be 75° during measurement. Ultraviolet-Visible-Near infrared (UV-VIS-NIR) spectroscopic properties of the as-grown and post-annealed samples were measured by SE (SC620 Shanghai Sanco, Inc.) in a range of 300–1000 nm. The incident angle was 60° and 70°, respectively.

For ellipsometric measurements, one can obtain the amplitude and phase of the complex reflectance ratio ρ ($=r_P/r_S$) for the parallel and perpendicular field components of the light beam, then the pseudo dielectric function $\langle\varepsilon\rangle$ of the sample can be obtained by the equation

$$\langle\varepsilon\rangle = \sin^2\phi + \sin^2\phi\tan^2\phi\frac{(1-\rho)^2}{(1+\rho)^2}, \quad (1)$$

where ϕ is the angle of incidence. The back surface of amorphous Al_2O_3 substrate was roughened to eliminate the component of the beam which was reflected from its backside. A three-phase model (ambient/MCN/Al_2O_3) was used to fit $\langle\varepsilon\rangle$. In the infrared range, we adopted a classical mid-infrared model to characterize the optical constants of the MCN films. In the UV-VIS-NIR range, we used widely accepted dispersion function Tauc–Lorentz (TL) model together with Lorentz model to characterize the dielectric function of the films.

III. RESULTS AND DISSCUSSION

A. Structural, morphological analysis and cation distribution

Figure 1 shows the XRD patterns of the as-grown (Sample S_A) and post-annealed (Sample S_P) MCN films. The XRD peaks are indexed by making reference to $NiMn_2O_4$ with the JCPDS card No. of 84–0542. Cubic spinel structures are observed for the two samples. The difference is that it presents a low crystallization for sample S_A, but highly (220) orientation appears for S_P after post annealing process. The full width half maximum of the (220) peak is about 0.3° for S_P, corresponding to an averaged grain size of ~30 nm estimated by Scherrer equation.

Figure 2(a) shows the AFM picture of the as-grown sample, where tiny grains are presented and densely formed. The root-mean-square roughness is about 11.5 Å over an area of $2 \times 2\ \mu m^2$. Fig. 2(b) illustrates the surface morphology of the post-annealed sample measured by SEM. One can clearly observe that the grain size of sample S_P is much larger than that of sample S_A, indicating better oxidation and crystalline status for S_P. The thickness of the film is estimated to be about 170 nm from the cross section image of sample S_P (Inset of Fig. 2(b)).

Fig. 3 displays the characteristic core-level spectra of Co 2p, Mn 2p, Ni 2p, and O 1s of the two samples. It is generally accepted that energy gap between the main lines and satellite peaks is highly related to the oxidation states of cations. The XPS spectra of Co 2p consist of two main lines ($2p_{3/2}$ at about 780 eV and $2p_{1/2}$ at about 796 eV) and two satellite peaks. According to Ref. 17, a satellite peak located at ~6 eV above the $2p_{3/2}$ main line is associated with Co^{2+} species while that at ~10 eV above the main line is associated with Co^{3+}. In Fig. 3(a), two distinguishable satellite peaks are observed at about 6 eV above the $2p_{3/2}$ and $2p_{1/2}$ main lines, respectively. It indicates that only Co^{2+} exists in the films.[17] In Fig. 3(b), the Mn 2p spectrum does not contain any shake-up feature at higher binding energy, suggesting the

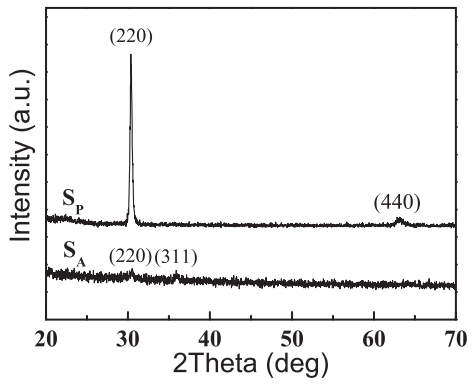

FIG. 1. XRD patterns of the as-grown (S_A) and post-annealed (S_P) MCN films.

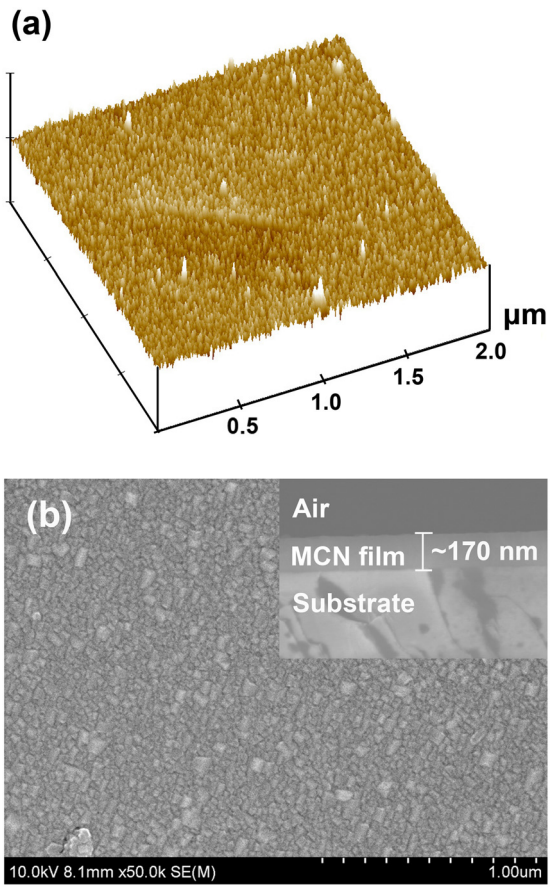

FIG. 2. AFM picture of the as-grown films deposited at 100 W (a) and SEM picture of the post annealed films deposited at 100 W (b). Inset: Cross section of SEM to measure the thickness of the film S_P.

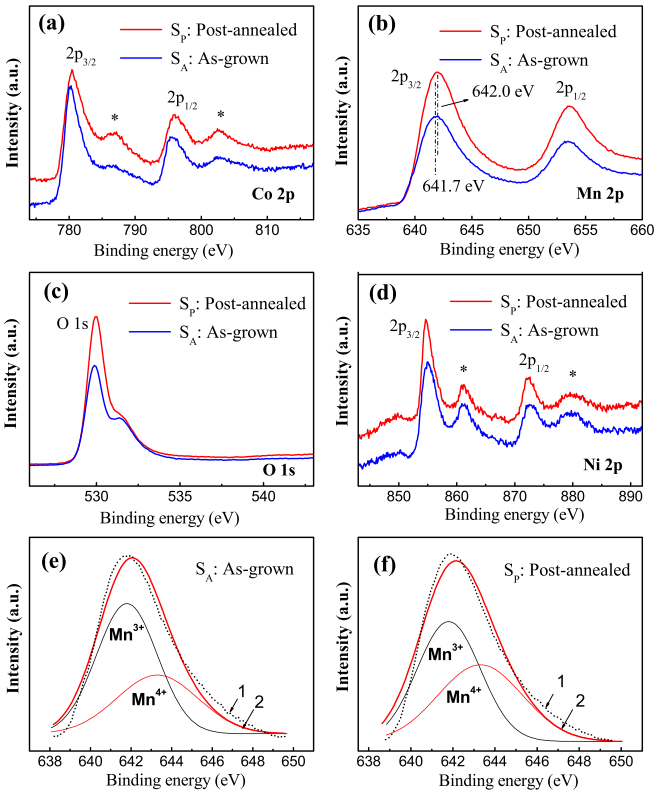

FIG. 3. XPS spectra of Co 2p (a), Mn 2p (b), O 1s (c), and Ni (2p) measured for as-grown and post-annealed samples, respectively. Asterisks denote the peak positions of satellite. Mn 2p signals of S_A (e) and S_P (f). 1: Experimental, 2: Calculated.

absence of Mn^{2+}.[18] It has been reported that the binding energies of Mn^{3+} and Mn^{4+} are 641.9 eV and 643.2 eV in Li-Co-Mn-O compounds.[19] The Mn $2p^{3/2}$ binding energy increases from 641.7 eV to 642.0 eV in our study, which means that the oxidation state of manganese ions increases after the post annealing process. The XPS spectra for Mn 2p signals of S_A and S_P can be deconvoluted after background subtraction by a fitting process of the Mn 2p signal using a Gaussian function, where the binding energies and FWHM values of Mn^{3+} and Mn^{4+} are referenced by $ZnMn_2O_4$ and $MgNiMnO_4$ compounds, respectively.[20] As shown in Figs. 3(e) and 3(f), the Mn 2p signal is fitted to optimize the intensities of the two peaks belonging to the Mn^{3+} and Mn^{4+} oxidation states after a least square procedure. The calculated Mn^{4+}/Mn^{3+} ratios for S_A and S_P are determined to be 0.52/0.88 and 0.65/0.75, respectively, indicating an increase in Mn^{4+}/Mn^{3+} ratio by 43% after the post-annealing process. The O 1s spectra show intense peak at about 529–530 eV accompanied by shoulders at higher binding energies (Fig. 3(c)). As shown in Fig. 3(d), the most intense peak of Ni $2p_{3/2}$ located at about 855.0 eV is characteristic of Ni^{2+} cation. Additionally, the appearance of shake-up feature at about 862 eV, a finger print of Ni^{2+} species, confirms the presence of Ni^{2+} cations.[21]

Therefore, we propose a molecule structure for the MCN thin film according to the oxidation states of the cations and charge balance relation

$$[Co^{2+}]_T[Ni^{2+}_{0.6}Mn^{3+}_{0.8+2\delta}Mn^{4+}_{0.6-2\delta}]_O O^{2-}_{4-\delta}, \quad (2)$$

where δ is the oxygen content.[22,23] The preferred sequence of cations to occupy an octahedral (O) site is assumed as: Mn^{4+}, $Ni^{2+} > Mn^{3+} > Co^{2+}$, where Ni^{2+}, Mn^{3+}, Mn^{4+} cations are unfavorable in tetrahedral (T) four-fold coordination. According to former studies, the as-grown sample is oxygen lacked by using RF deposition method when the working gas is pure argon.[24] According to the quantitative results from XPS spectra, we believe that the oxidation status and stoichiometry of the MCN films are improved by the post-annealing process. This viewpoint can be further convinced by the later results of the infrared optical constants.

B. Infrared optical constants

A classical mid-infrared dispersion relation can be applied to describe the infrared dielectric function of the MCN films. A complex dielectric function for N cells per unit volume is given by[25]

$$\varepsilon_1 = \varepsilon_\infty - \frac{Nq^2}{M^*\varepsilon_0}\frac{\tau^2}{1+\omega^2\tau^2}, \quad (3a)$$

$$\varepsilon_2 = \frac{Nq^2}{M^*\varepsilon_0}\frac{\tau}{\omega(1+\omega^2\tau^2)}, \quad (3b)$$

where ε_∞ is the high-frequency dielectric constants, M^* is the reduced mass of cations and anions in a unit cell, q is the ionic average effective charge, ω is the incident infrared frequency, and τ is an energy-independent relaxation time. Meanwhile the optical constants including refractive index n and extinction coefficient k are determined as follows:

$$n = (1/\sqrt{2})\sqrt{\sqrt{\varepsilon_1^2+\varepsilon_2^2}+\varepsilon_1}, \quad (4a)$$

$$k = (1/\sqrt{2})\sqrt{\sqrt{\varepsilon_1^2+\varepsilon_2^2}-\varepsilon_1}. \quad (4b)$$

The ellipsometric spectra are analyzed by a three layer model (Air/MCN film/Al_2O_3). The optical constants of Al_2O_3 in the fitting are taken from Ref. 26. Schematic structure of the three layer model is shown in the inset of Fig. 4(a).

Fig. 4 shows the measured and fitted ellipsometric spectra at the incident angle of 75° in the wavelength range of 2.8–6.7 μm, respectively. A best fit is obtained to the experimental data in the entire wavelength range. Fig. 5 shows the obtained refractive index n and extinction coefficient k. The refractive index decreases with increasing wavelength, but the extinction coefficient increases monotonously. The refractive indices of both samples reach their maximum of about 2.56 at 2.8 μm, and the minimal values are 2.42 and 2.35, respectively, for S_A and S_P at 6.7 μm. The maximal k value for the two samples are about 0.045 (S_A) and 0.051 (S_P) at 6.7 μm. The high frequency dielectric constant ε_∞ is close to each other for S_A and S_P. They are 6.72 and 6.77, respectively. The derived thicknesses are coincident with the value measured by the SEM cross section picture. Furthermore, the static charge can be calculated based on the fitted coefficient $Nq^2/M^*\varepsilon_0$. It is an intuitive concept to

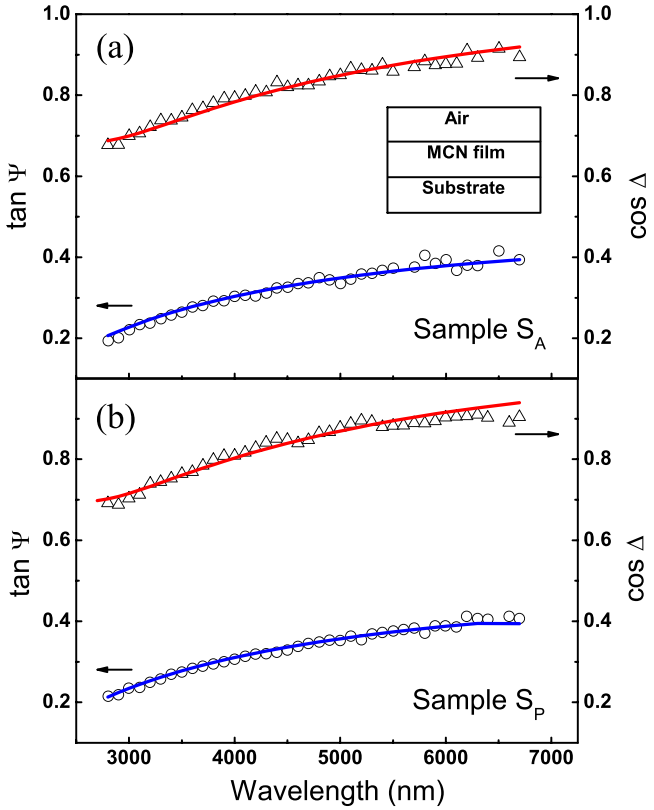

FIG. 4. Measured and fitted parameters in the range of 1500–3600 cm^{-1} (2.8–6.7 μm) for S_A and S_P.

partition the ground state electronic charge into different atoms. The derived average effective charge of oxygen atoms is -1.84 ± 0.14 for the as-grown sample and -2.23 ± 0.07 for the post-annealed one, suggesting that the oxidation status and stoichiometry has been improved after the post-annealing process. All parameters of analysis on infrared properties are summarized in Table I.

C. Dielectric function and optical absorption properties in UV-VIS-NIR range

To fit the optical properties in UV-VIS-NIR range, we use widely accepted dispersion function TL model together with a double Lorentz model.[27–29]

A double Lorentz dispersion function can be expressed as

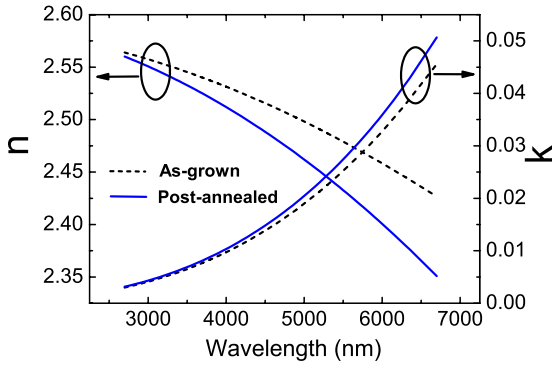

FIG. 5. Measured refractive index n and extinction coefficient k in the wavelength range of 2.8–6.7 μm.

TABLE I. Fitting values of mid-infrared model for the as-grown and post-annealed MCN films.

Sample	ε_∞	$\sqrt{\frac{Nq^2}{M^*\varepsilon_0}}$ ($\times 10^3$ cm^{-1})	$\tau(10^{-14}$ s)	Film thickness (nm)
As-grown (S_A)	6.72 ± 0.07	1.41 ± 0.11	0.0075	178 ± 5
Post-annealed (S_P)	6.77 ± 0.04	1.71 ± 0.05	0.0105	174 ± 3

$$\begin{aligned}\tilde{\varepsilon}(E) &= \varepsilon_1(E) + i\varepsilon_2(E) \\ &= \sum_{j=1}^{2} \frac{A_j B_j E_{nj}(E_{nj}^2 - E^2)}{(E_{nj}^2 - E^2)^2 + B_j{}^2 E^2} \\ &\quad + i \cdot \sum_{j=1}^{2} \frac{A_j B_j^2 E_{nj} E}{(E_{nj}^2 - E^2)^2 + B_j^2 E^2}\,. \end{aligned} \tag{5}$$

Equation (5) depends on three parameters: The amplitude A_j, the peak transition energy E_{nj}, and broadening term B_j.

The TL dispersion function can be expressed as

$$\varepsilon_2(E) = \begin{cases} \dfrac{AE_nC(E-E_g)^2}{(E^2-E_n^2)^2 + C^2E^2}\dfrac{1}{E} & (E > E_g) \\ 0 & (E \le E_g) \end{cases}, \tag{6}$$

where Eq. (6) is related to four parameters: The transition matrix element A, the peak transition energy E_n, the broadening term C, and the band gap energy E_g. The real part ε_1 is the result of self consistent *Kramers–Kronig* integration of ε_2

$$\varepsilon_1(E) = \varepsilon_{offset} + \frac{2}{\pi} P \int_{E_g}^{\infty} \frac{\xi \varepsilon_2(E)}{\xi^2 - E^2} d\xi\,, \tag{7}$$

where ε_{offset} is an offset component of the dielectric constant.

By applying a double Lorentz model and a TL model, we can retrieve the imaginary part (ε_2) of the dielectric functions of the two samples. Fig. 6 shows the measured and

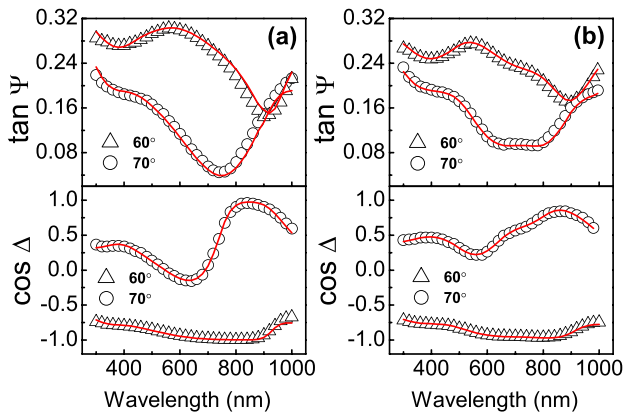

FIG. 6. Measured (dotted line) and fitted (straight line) ellipsometric spectra Ψ and Δ of MCN films at the incident angles of 60°, 70° (a) sample S_A, (b) sample S_P.

TABLE II. Parameter values of double Lorentz plus TL model for the samples. T_f is the thickness of the films.

Samples	S_A	S_P
A_1	1.2 ± 0.2	0.74 ± 0.06
E_{n1} (eV)	2.60 ± 0.03	2.44 ± 0.01
B_1 (eV)	1.3 ± 0.2	0.70 ± 0.05
A_2	3.7 ± 0.1	3.42 ± 0.07
E_{n2} (eV)	4.4 ± 0.6	7.4 ± 0.6
B_2 (eV)	5.2 ± 0.2	10.0 ± 0.4
A_3	33.1 ± 0.7	7.4 ± 1.0
C (eV)	0.50 ± 0.08	0.55 ± 0.02
E_{n3} (eV)	1.30 ± 0.05	1.52 ± 0.01
E_{g3} (eV)	1.27 ± 0.02	1.14 ± 0.03
ε_{offset}	2.5 ± 0.2	1.2 ± 0.2
T_f (nm)	167.6 ± 0.6	170.5 ± 0.4

fitted spectra at the incident angle of 60°, 70° in 300 nm–1000 nm wavelength range. For clarity, only one out of every four measured data points is shown. An excellent agreement is achieved between the experimental and fitted spectra for the two samples in the entire range. All fitted parameters are shown in Table II.

Fig. 7 shows the obtained imaginary part of the dielectric constants of sample S_A and S_P in UV-VIS-NIR range. Three absorption structures are observed located at about 1.7 eV, 2.4–2.6 eV, and 3.5–4.0 eV, respectively. The absorption mechanism is complex in spinel materials. The main origination is crystal field (CF) d-d or intraelectronic transitions, charge-transfer (CT) transitions, or metal-metal intervalence transitions.[30,31] Our results can be interpreted in terms of the CT transitions involving 2p electrons of oxygen ions and 3d electrons of Mn and Co ions. According to the results of XPS and infrared optical constants, the oxidation status of Mn ions has been changed after the post-annealing process. Furthermore, the CT transition energy for Mn^{4+} is lower than that of Mn^{3+}, due to higher binding energy caused by stronger Coulomb attraction between Mn^{4+} cation and the d electrons.[30,32] The increase of Mn^{4+} concentration enhances the absorption peak at ~1.7 eV apparently, but reduces that at around 3.5–4.0 eV. In terms of the absorption structure of CT transition at about 1.9 eV from O^{2-} (2p) to Mn^{4+} (3d) in $LiNi_xMn_{2-x}O_4$ films,[30] we attribute the structure at 1.7 eV to the CT transition involving O^{2-} (2p) and Mn^{4+} (3d) ions. Then, the absorption at 3.5–4.0 eV is mainly attributed to the CT transition of O^{2-} (2p)–Mn^{3+} (3d). Finally, the absorption structure at 2.4–2.6 eV can be interpreted as being due to O^{2-} (2p) to Co^{2+} (3d) transition, according to the optical absorption structure in Co_3O_4.[31]

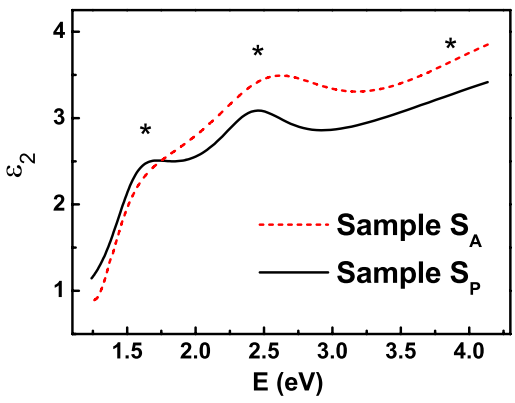

FIG. 7. Imaginary parts of dielectric functions measured by SE. Asterisks denote positions of the absorption peaks.

IV. CONCLUSION

We have prepared MCN films on alumina substrate with cubic spinel structures by RF sputtering deposition method. Cation distribution in the MCN films has been estimated based on the XPS results. Both Mn^{3+} and Mn^{4+} are found to be existed and the Mn^{4+}/Mn^{3+} ratio increases after the post annealing process. The optical constants of MCN sample are affected by oxidation states of the MCN sample. The average effective charge has been obtained based on infrared optical constants, which convinces the improvement in stoichiometry due to post-annealing process. Broad absorption peaks located at 1.7 eV and 3.5–4.0 eV are believed to be mainly owing to the transitions of O^{2-} to Mn^{4+} and Mn^{3+}, respectively. Absorption peaks at 2.4–2.6 eV is believed to be the transition of O^{2-} to Co^{2+}. Our results are helpful to understand the mechanism of its optical absorption process, as well as the development of optoelectronic device based on MCN films.

ACKNOWLEDGMENTS

This work was supported by National Natural Science Foundation (Grant Nos. 11204336, 61274138, and 11304336) and Shanghai Project (Grant No. 12ZR1452200).

[1]A. Zimmers, L. Aigouy, M. Mortier, A. Sharoni, S. M. Wang, K. G. West, J. G. Ramirez, and I. K. Schuller, Phys. Rev. Lett. **110**, 056601 (2013).
[2]C. J. Zhang and H. Oyanagi, Phys. Rev. B **79**, 064521 (2009).
[3]K. Jin, N. P. Butch, K. Kirshenbaum, J. Paglione, and R. L. Greene, Nature **476**, 73 (2011).
[4]C. L. Lu, X. Chen, S. Dong, K. F. Wang, H. L. Cai, J. M. Liu, D. Li, and Z. D. Zhang, Phys. Rev. B **79**, 245105 (2009).
[5]J. Wu, Z. M. Huang, Y. Hou, Y. Q. Gao, and J. H. Chu, Appl. Phys. Lett. **96**, 082103 (2010).
[6]L. He and Z. Y. Ling, J. Appl. Phys. **110**, 093708 (2011).
[7]L. He and Z. Y. Ling, Appl. Phys. Lett. **98**, 242112 (2011).
[8]Y. Q. Gao, Z. M. Huang, Y. Hou, J. Wu, Y. J. Ge, and J. H. Chu, Appl. Phys. Lett. **94**, 011106 (2009).
[9]T. Yokoyama, T. Meguro, Y. Shimada, J. Tatami, K. Komeya, and Y. Abe, J. Mater. Sci. **42**, 5860 (2007).
[10]R. Schmidt and A. W. Brinkman, Adv. Funct. Mater. **17**, 3170 (2007).
[11]Y. Hou, Z. M. Huang, Y. Q. Gao, Y. J. Ge, J. Wu, and J. H. Chu, Appl. Phys. Lett. **92**, 202115 (2008).
[12]L. He, Z. Y. Ling, Y. T. Huang, and Y. S. Liu, Mater. Lett. **65**, 1632 (2011).
[13]G. H. Lei, H. W. Chen, S. X. Zheng, F. Z. Lou, L. L. Chen, L. Zeng, J. H. Zhang, Q. Zhao, and C. R. Yang, J. Mater. Sci.: Mater. Electron. **24**, 1203 (2013).
[14]S. A. Kanade and V. Puri, Mater. Lett. **60**, 1428 (2006).
[15]G. Ji, A. M. Chang, J. B. Xu, H. M. Zhang, J. Hou, B. Zhang, and P. J. Zhao, Mater. Lett. **107**, 103 (2013).
[16]R. Dannenberg, S. Baliga, R. J. Gambino, A. H. King, and A. P. Doctor, J. Appl. Phys. **86**, 2590 (1999).
[17]W. F. Wei, W. X. Chen, and D. G. Ivey, Chem. Mater. **20**, 1941 (2008).
[18]H. R. Chen, X. P. Dong, J. L. Shi, J. J. Zhao, Z. L. Hua, J. H. Gao, M. L. Ruan, and D. S. Yan, J. Mater. Chem. **17**, 855 (2007).
[19]K. M. Shaju, G. V. S. Rao, and B. V. R. Chowdari, Solid State Ionics **152**, 69 (2002).
[20]J. Topfer, A. Feltz, D. Graf, B. Hackl, L. Raupach, and P. Weissbrodt, Phys. Status Solidi A **134**, 405 (1992).

[21]J. F. Marco, J. R. Gancedo, M. Gracia, J. L. Gautier, E. I. Rios, H. M. Palmer, C. Greaves, and F. J. Berry, J. Mater. Chem. **11**, 3087 (2001).
[22]P. N. Lisboa, M. Bahout, P. Barahona, C. Moure, and O. Pena, J. Phys. Chem. Solids **66**, 1206 (2005).
[23]R. Schmidt, A. Basu, and A. W. Brinkman, Phys. Rev. B **72**, 115101 (2005).
[24]R. Dannenberg, S. Baliga, R. J. Gambino, A. H. King, and A. P. Doctor, J. Appl. Phys. **86**, 514 (1999).
[25]Z. M. Huang, Z. H. Zhang, C. P. Jiang, J. A. Yu, J. L. Sun, and J. H. Chu, Appl. Phys. Lett. **77**, 3651 (2000).
[26]E. D. Palik, *Handbook of Optical constants of Solids* (Academic, New York, 1998), p. 653.
[27]G. E. Jellison and F. A. Modine, Appl. Phys. Lett. **69**, 371 (1996).
[28]Z. G. Hu, J. H. Ma, Z. M. Huang, Y. N. Wu, G. S. Wang, and J. H. Chu, Appl. Phys. Lett. **83**, 3686 (2003).
[29]H. Fujiwara and M. Kondo, Phys. Rev. B **71**, 075109 (2005).
[30]K. J. Kim and J. H. Lee, Solid State Commun. **141**, 99 (2007).
[31]K. J. Kim and Y. R. Park, Solid State Commun. **127**, 25 (2003).
[32]L. B. Zhang, Y. Hou, W. Zhou, Y. Q. Gao, J. Wu, Z. M. Huang, and J. H. Chu, Solid State Commun. **159**, 32 (2013).